SYSTEMS, SCIENCE AND SOFTWARE

SSS-R-77-3191

SEISMIC STUDIES FOR IMPROVED YIELD DETERMINATION

T. G. Barker
M. Baker
P. Coleman
D. G. Lambert

Quarterly Technical Report
For Period January 1 - March 31, 1977

Sponsored by
Advanced Research Projects Agency
ARPA Order No. 2551

This research was supported by the Advanced Research Projects Agency of the Department of Defense and was monitored by AFTAC/VSC, Patrick AFB, FL 32925, under Contract No. F08606-76-C-0041.

April 1977

P. O. BOX 1620, LA JOLLA, CALIFORNIA 92038, TELEPHONE (714) 453-0060

AFTAC Project Authorization No. VELA/T/7712/B/ETR

Program Code No. 6H189

Effective Date of Contract: October 1, 1976

Contract Expiration Date: September 30, 1977

Amount of Contract: 410,412

Contract No. F08606-76-C-0041

Principal Investigator and Phone No.
Dr. Thomas C. Bache, (714) 453-0060, Ext. 337

Project Scientist and Phone No.
Dr. Ralph W. Alewine, III, (202) 325-8484

UNCLASSIFIED

SECURITY CLASSIFICATION OF THIS PAGE (When Data Entered)

REPORT DOCUMENTATION PAGE		READ INSTRUCTIONS BEFORE COMPLETING FORM
1. REPORT NUMBER	2. GOVT ACCESSION NO.	3. RECIPIENT'S CATALOG NUMBER
4. TITLE (and Subtitle) SEISMIC STUDIES FOR IMPROVED YIELD DETERMINATION.		5. TYPE OF REPORT & PERIOD COVERED Quarterly Technical Report 1 Jan 1977 - March 31, 1977
		6. PERFORMING ORG. REPORT NUMBER SSS-R-77-3191
7. AUTHOR(s) T. G. Barker, M. Baker, P. Coleman and D. G. Lambert		8. CONTRACT OR GRANT NUMBER(s) F08606-76-C-0041
9. PERFORMING ORGANIZATION NAME AND ADDRESS Systems, Science and Software P. O. Box 1620 La Jolla, California 92038		10. PROGRAM ELEMENT, PROJECT, TASK AREA & WORK UNIT NUMBERS Program Code No. 6H189 ARPA Order No. 2551
11. CONTROLLING OFFICE NAME AND ADDRESS VELA Seismological Center 312 Montgomery Street Alexandria, VA 22314		12. REPORT DATE April 1977
		13. NUMBER OF PAGES 47
14. MONITORING AGENCY NAME & ADDRESS (if different from Controlling Office)		15. SECURITY CLASS. (of this report) Unclassified
		15a. DECLASSIFICATION/DOWNGRADING SCHEDULE

16. DISTRIBUTION STATEMENT (of this Report)

Approved for Public Release, Distribution Unlimited.

17. DISTRIBUTION STATEMENT (of the abstract entered in Block 20, if different from Report)

18. SUPPLEMENTARY NOTES

19. KEY WORDS (Continue on reverse side if necessary and identify by block number)

Explosion Source Modeling, Yield Determination, Cratering Explosions, Theoretical Seismogram Generation

20. ABSTRACT (Continue on reverse side if necessary and identify by block number)

The report summarizes the results of the second three months of research on a contract whose main objective is to examine the parameters that effect the seismic signals from underground nuclear explosions. Results were presented on research in five areas: 1. Data pertinent to regional bias in m_b and M_s in the United States and central Asia were summarized; 2. Signals simulating those from multiple explosions were decomposed and scaled by narrow-band filtering methods; 3. Numerical simulations of contained explosions were compared with previous laboratory

DD FORM 1 JAN 73 1473 EDITION OF 1 NOV 65 IS OBSOLETE

UNCLASSIFIED

SECURITY CLASSIFICATION OF THIS PAGE (When Data Entered)

simulations; 4. Laboratory experiments of cratering explosions were completed using 0.25 gram charges embedded in concrete; 5. The primary factors controlling amplitude-yield scaling at regional distances were investigated.

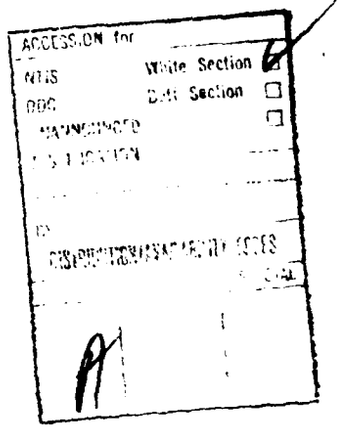

TABLE OF CONTENTS

I. SUMMARY

The objective of our research program is to examine the parameters that affect the seismic signals from underground explosions. Our attention is primarily directed to those features of the seismic waveforms that reliably indicate the explosion yield. Our research program includes empirical studies of the available data, experimental studies using small charges to simulate explosions and the development and application of theoretical and numerical methods. Emphasis is on the latter, in particular we are applying techniques for numerically simulating the far-field signals from both contained and cratering underground explosions. The numerical simulation techniques represent a synthesis of the finite difference methods for computing ground motion in the near-source large displacement regime and the efficient wave propagation techniques of theoretical seismology.

During the second three-month period of our present contract, our research has been conducted in a number of areas. These areas and the major results obtained in each are summarized in the following paragraphs.

An important problem engaging our attention during most of this quarter was an attempt to understand and explain the coupling differences between explosions in different source materials (granite, salt, saturated tuffs and rhyolites). Considerable attention was given to the effect of changing overburden pressure for explosions at different depths. Many of the important results obtained were presented orally at several DoD meetings during the quarter. We are now preparing a special report in which our current understanding of m_b and M_s scaling with yield and source material will be summarized, but these results are not yet ready for publication in this quarterly report.

A number of research efforts were brought to completion, or nearly so, during the quarter. This report is devoted to a summary of these investigations. We reviewed the published evidence bearing on the nature and variability of the anelastic attenuating properties of the earth's upper mantle, and a topical report [Mitchell and Bache, 1977] was submitted. We conclude that the published evidence strongly suggests the presence of a low velocity, high attenuation zone in the upper mantle beneath the western United States. This zone appears to be weak or absent beneath the eastern United States and central Asia. The presence of such a low velocity zone is expected to significantly lower m_b values compared to values from events in areas where it is absent. However, the effect on M_s should be quite small.

A study of multiple explosions and the application of certain signal analysis techniques to separate the individual events was brought to completion this quarter and a topical report [Lambert, 1977] is being prepared. The object of this study was to simulate multiple explosions by summing near-field ground motion recordings of NTS explosions and then attempt to identify and scale the individual events by analyzing the composite signal. Using recordings of the large Pahute Mesa events MAST, COLBY and POOL, realistic multiple explosion signals were generated. These signals were processed by our program MARS (Multiple Arrival Recognition System) which uses Hilbert transform envelopes from narrow band filter output to separate individual phase arrivals in a signal. Using close-in instruments, we were able to identify and scale the individual arrivals down to quite small time separations. Separation times can be resolved as long as reasonable signal power (signal/noise > 1) is present at frequencies greater than 3.5 divided by the separation time. For example, if good signal is present at 35 Hz, phase

arrivals separated by 0.1 seconds can be separated. The results studied were from simulated single station recordings of a multiple event. For an actual event, it would be desirable to employ an array of stations. Analysis of such data using MARS should allow identification and scaling (by yield) of the individual events in the multiple explosion array.

We have been conducting an experimental program in which small-scale modeling of underground nuclear explosions is being simulated. The tests have been conducted in grout cylinders and the explosives are 0.25 grams of PETN, which are carefully manufactured to be spherically symmetric sources. In our last quarterly report we described the results of the first set of experiments in which the explosions were fully contained. A second set of experiments was then carried out in which the explosions were at cratering depths.

One important reason for doing the experiments described in the previous paragraph was to provide a carefully controlled data set for testing and validating our numerical modeling procedures. We have modeled the contained explosions using a one-dimensional finite difference code. The code and the constitutive model are the same as we use for modeling underground nuclear explosions. For these one-dimensional experiments the computed "ground motion" time histories agree very well with the experimental data. This provides important validation of our computational procedures. We are now engaged in modeling the cratering experiments.

Most of our work on the ground motion amplitude-yield scaling for underground explosions has been directed toward explaining the teleseismic (>2000 km) data. It has long been known that the increase in amplitude with yield is markedly less for regional (50-500 km) body wave amplitude than for teleseismic body waves. This is important for two reasons.

First, any satisfactory model should be able to explain all the data. Second, the regional body wave data sample a different portion of the source spectrum than other data and represent another opportunity to validate calculations of source coupling. For these reasons we have made a preliminary study of the theoretical amplitude-yield scaling for the regional data. We find that our models indeed predict a lower slope for the amplitude-yield curve in this region. The primary reason is that the regional data are higher frequency and see the portion of the source spectrum beyond the corner frequency. This effect is more pronounced at higher yields than at lower yields, thus decreasing the amplitude-yield slope.

II. INTRODUCTION

The primary objective of the research program is to systematically examine the parameters that control magnitude-yield relationships for underground nuclear explosions. During the second three-month period of this contract, research has been conducted in the following areas:

1. A review of the evidence for variability in the attenuating properties of the upper mantle between Eurasia and North American (summarized in Section 3.1).
2. A study of the utility of our signal analysis program (MARS) for decomposing and scaling the individual events in a multiple explosion array (summarized in Section 3.2).
3. A laboratory simulation of contained and cratering explosions using small (0.25 gm) charges in grout cylinders (summarized in Section 3.3).
4. A finite difference numerical modeling of the experiments in 3 and comparison of observed and computed data (summarized in Section 3.4).
5. A study of the amplitude-yield scaling properties for large underground explosions recorded at regional distances (summarized in Section 3.5).

During this quarter we also made oral presentations at several Department of Defense (DoD) meetings. These presentations were mostly devoted to our work on the coupling of explosions in various source materials and the significance of coupling differences for m_b and M_s. This work is

central to our contract effort and most of our attention was devoted to these issues. A report summarizing the current state of our understanding of M_b and M_s from explosions is now in preparation.

The remainder of the report is devoted to technical discussions of results in the five areas enumerated above.

III. TECHNICAL DISCUSSION

3.1 EVIDENCE BEARING ON THE NATURE OF THE ANELASTIC PROPERTIES OF THE UPPER MANTLE BENEATH NORTH AMERICA AND EURASIA

During this quarter, a topical report [Mitchell and Bache, 1977] was prepared summarizing work relating to the seismic attenuation characteristics of the western United States compared with those of the eastern U.S. and central Asia. The report cites previously published evidence supporting the existence of a low velocity, high attenuation (low Q) zone in the upper-mantle beneath the western U.S. (especially beneath the Basin and Range Province) and the lack of such a zone in the eastern U.S. and central Asia. In this section we summarize the main conclusions of that report.

Models of seismic velocity and Q inferred from data for the eastern U.S. require a thin, poorly developed low velocity zone or none at all. The evidence is based upon long seismic profiles for P waves (reproduced in Figure 3.1 from Masse [1973]), surface wave dispersion, and travel time residuals for teleseismic body waves. The absence of a low Q zone is consistent with an attenuation study done for the upper mantle beneath the eastern U.S. (see Figure 3.2, from Lee and Solomon [1975]).

Data taken in the western U.S. include P and S wave amplitudes and travel time residuals from teleseisms, PL-P, travel time residuals, regional short-period attenuation measurements (from the nuclear explosion SALMON), and surface wave attenuation and dispersion. It is pointed out in the report that in North America, low velocity and low Q zones in the upper mantle coincide. Also, seismic velocities found in the low velocity zones are too high to be explained by mineralogical or temperature gradients. The low velocities are more likely due to partial melting or water in the upper

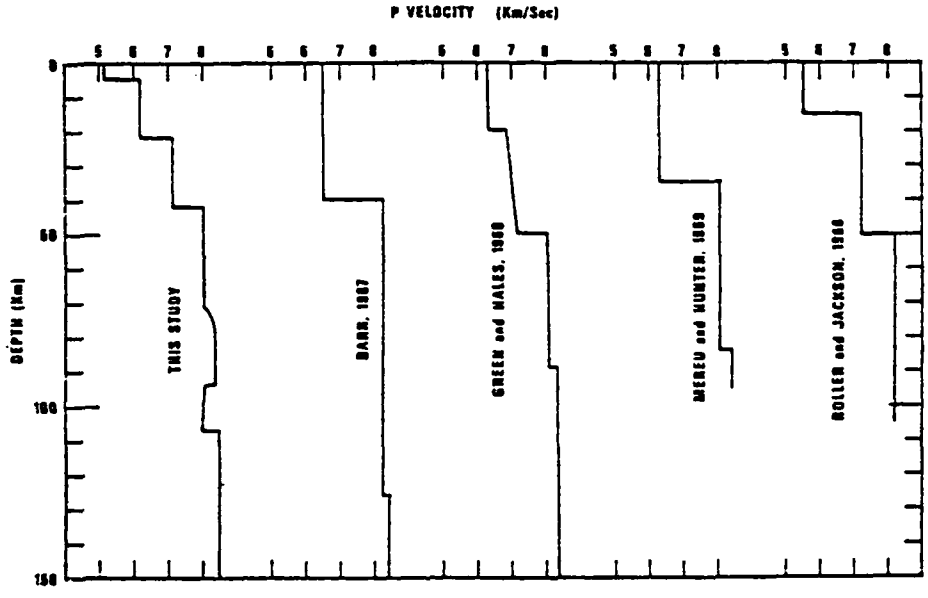

Figure 3.1. P wave velocity models for eastern North America (from Masse [1973]), reproduced with permission from Bull. Seism. Soc. Am.).

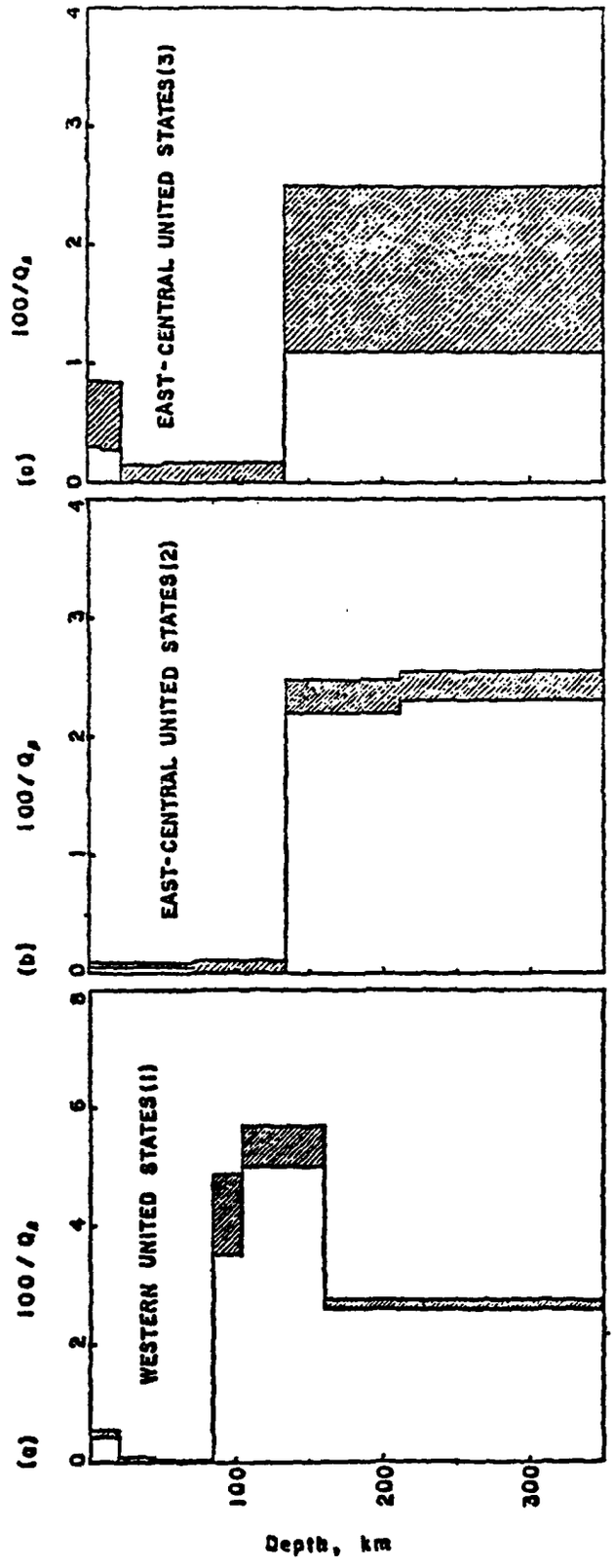

Figure 3.2. Attenuation models for the eastern and western United States. The shaded regions indicate the envelope of models which are consistent with each data set (after Lee and Solomon [1975], reproduced with permission from Geophys. J. Roy. astr. Soc.).

mantle, both of which result in higher attenuation. All body wave data cited (see Figure 3.3) support the existence of a low velocity, low Q zone, as do surface wave data for periods less than 15 seconds. Surface wave amplitudes for periods greater than 15 seconds do not exhibit any regional variation, and thus M_s measurements should not vary from east to west in the U.S. From this evidence it is difficult to estimate the extent to which values of m_b will vary, but low Q zones inferred are sufficient to appreciably lower m_b values in the western U.S. It is also expected that waves entering the western U.S. from teleseismic distances would be further attenuated elastically by the seismic velocity contrast between the low velocity zone and its upper boundary. Measurements of high heat flow and electrical conductivity are cited as further evidence of the anomalous nature of the upper mantle beneath the western U.S.

Although data for central Asia and northern Europe are sparse, they suggest that this region is characteristic of a tectonically stable area. Love wave group velocities were found to be much higher than in the neighboring active Himalayas and Tibetan Plateau. Rayleigh wave attenuation is similar to that in eastern North America. These and other data suggest the absence of a low velocity, low Q zone beneath Eurasia.

It is concluded that the evidence indicates the presence of a low velocity, low Q zone in the western U.S. but not in the eastern U.S. and stable areas of Eurasia. This zone is expected to affect measurements of M_s very little, but those of m_b by an appreciable amount.

3.2 SIMULATION AND DECOMPOSITION OF MULTIPLE EXPLOSION SEISMOGRAMS

Lambert, et al. [1976] and Savino, et al. [1976] describe the results of some experiments on the separation and

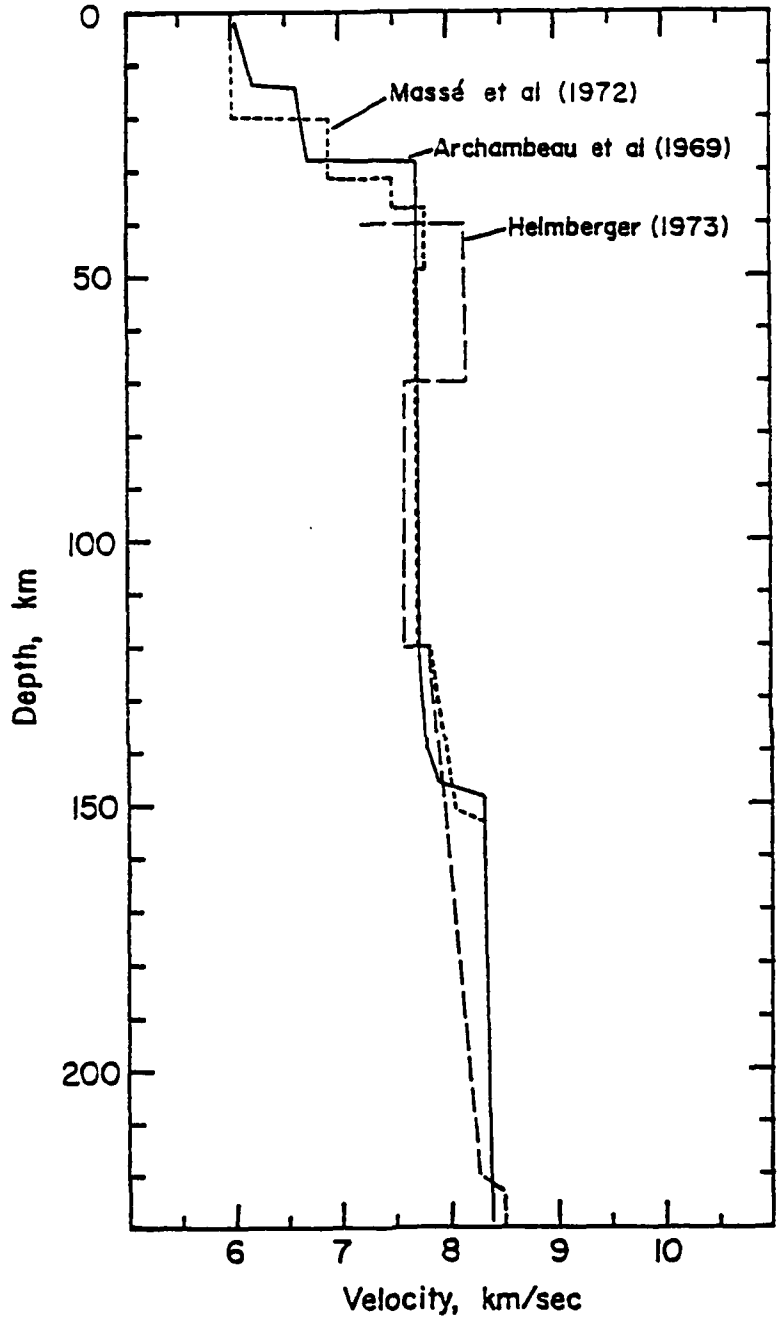

Figure 3.3. P wave velocity models for western North America.

scaling of individual events from seismic records of multiple explosions. Herein we summarize the continuation of that work. A detailed report on this research will be given in a topical report in preparation. The purpose of the study was to simulate signals from multiple explosions and to develop techniques to identify the separate events.

The techniques used to decompose signals from multiple events are based on applying a sequence of narrow-band filters over a range of center frequencies to these signals (see Lambert, et al., 1976, for details). For each center frequency, the filtered output provides a display of the phase (relative arrival times) and amplitude information at that frequency. Resolution of smaller time difference requires high center frequencies. The following discussion briefly describes two examples of our most recent applications of these techniques to multiple explosions.

In our most recent work we simulated signals from a multiple event for which all signals traversed a common propagation path (Case I) and for which the propagation paths were different (Case II). Since we have no seismograms for an actual multiple event, we modeled the situation in Case I by using records of a single shot at a set of stations as though they were a set of shots recorded at a single station. That is, the records from the stations were simply added together to form a composite seismogram, which was then analyzed to extract the constituent arrivals.

The events used for Case I were the Pahute Mesa events MAST and COLBY. The shot-station geometry is depicted in Figure 3.4. Figure 3.5 shows the composite signals and corresponding Hilbert transform envelope sums (see Lambert, et al., 1976) for various combinations of records for the MAST event. The arrival times at the respective stations are indicated on the envelope sum plots. The signals

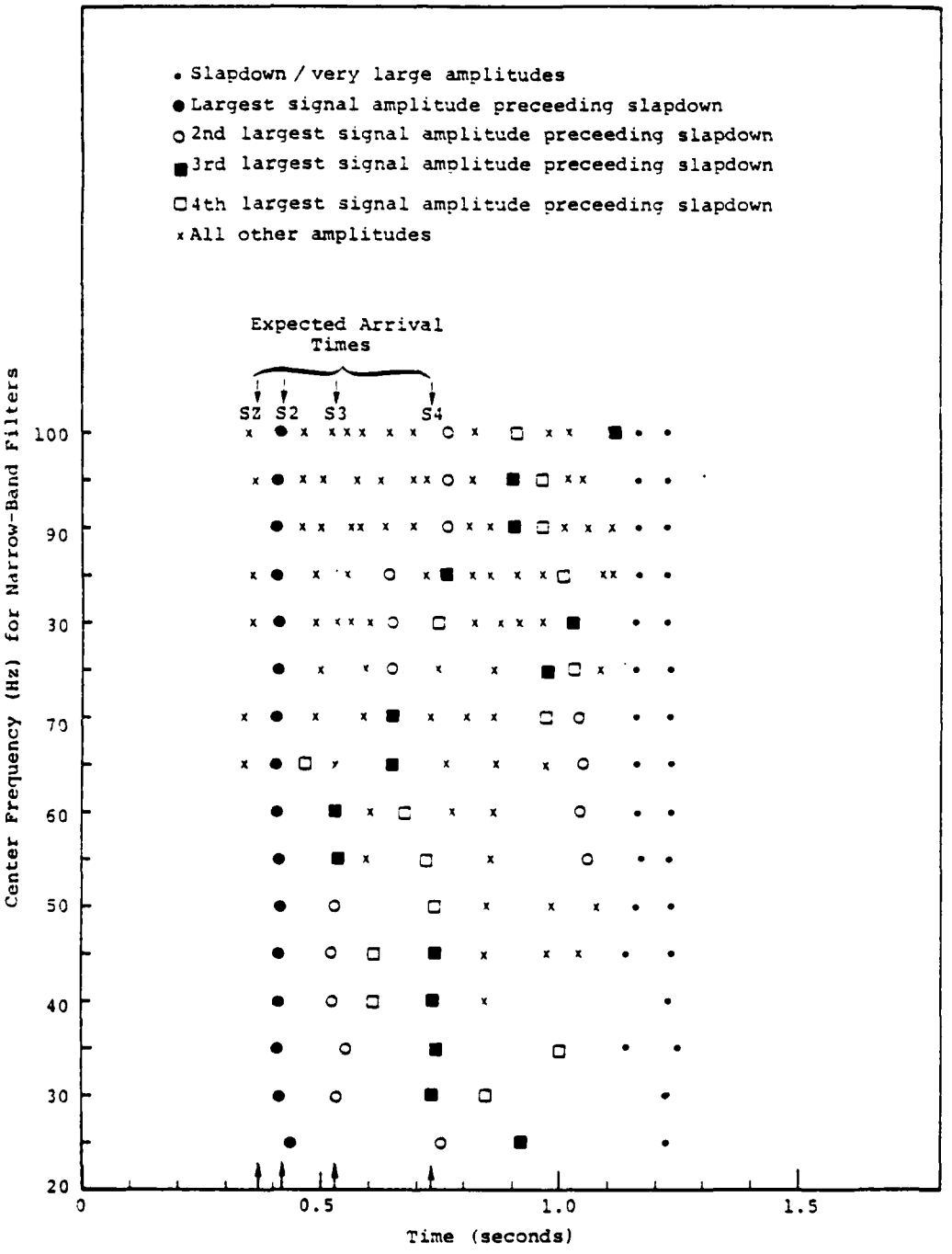

Figure 3.4. The narrow-band filter output for the multiple event composed from MAST records SZ, S2, S3 and S4 is displayed. The peaks of the envelope are plotted versus arrival time for each filter. The amplitudes of these peaks are indicated by the symbols described in the legend.

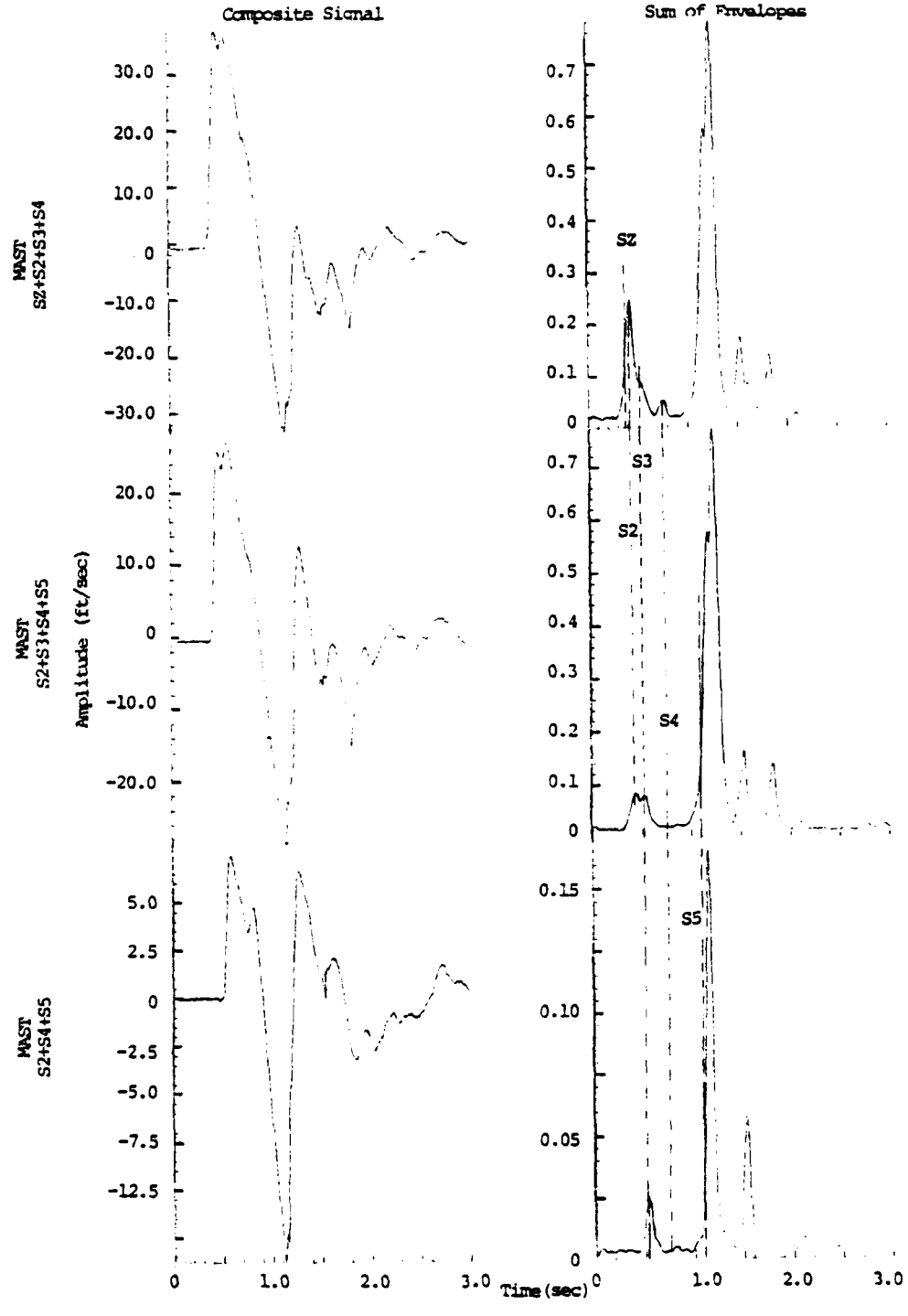

Figure 3.5. Composite signals (left column) and Hilbert transform envelopes for different combinations of recording stations. The onset time at the stations is indicated in the envelope sum plots.

corresponding to the arrivals at SZ/S2, S3 and S4 are seen as distinct bumps on at least one of the envelope sums. The difference in arrival times between SZ and S2 is too small (0.05 second) to be resolved on this plot. The large spikes at the S5 arrival time are due to spall closure and obscure the S5 arrival. To further decompose the composite seismograms, we refer to the narrow-band filter outputs shown in Figure 3.6. A coherent event is identified as a peak (identified by various symbols on the figure) which persists at several adjacent frequencies and times. For example, the event labeled "largest amplitude preceding slap-down" shows at the same time for each frequency. Note that for high frequencies, an event preceding the largest before slap-down emerges. This has the travel time for SZ and we see that the technique has resolved the S2 and SZ arrivals. In general, our results show that separation of separate arrivals becomes possible when the narrow-band center frequencies are above about 3.5/T, where T is the difference in arrival times. Various other coherent arrivals may be seen on this plot that may be attributed to propagation path effects. Other interpretations and analyses for different composite seismograms are discussed in the topical report now in preparation.

We proceed now to Case II, where seismograms from several events were used to make up simulated multiple explosion records. We used the events MAST, COLBY and POOL. The stations used for COLBY and POOL were on a line between the shot points and thus are likely to have aspects of their travel path in common. The travel path to MAST, on the other hand, is likely to be rather different. Figure 3.7 shows the geometry for this problem. The stations are positioned in a line according to the distance from their respective sources. As in Case I, we plot the composite and envelope sums (Figure 3.8) with the arrival times indicated on the plot. One can see distinct

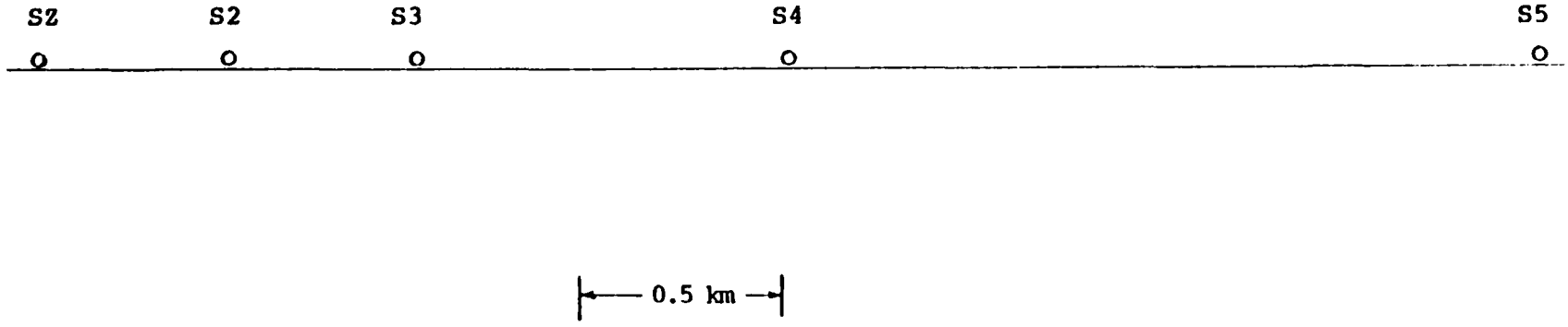

Figure 3.6. Vertical section of geometry for near-field recording of MAST.

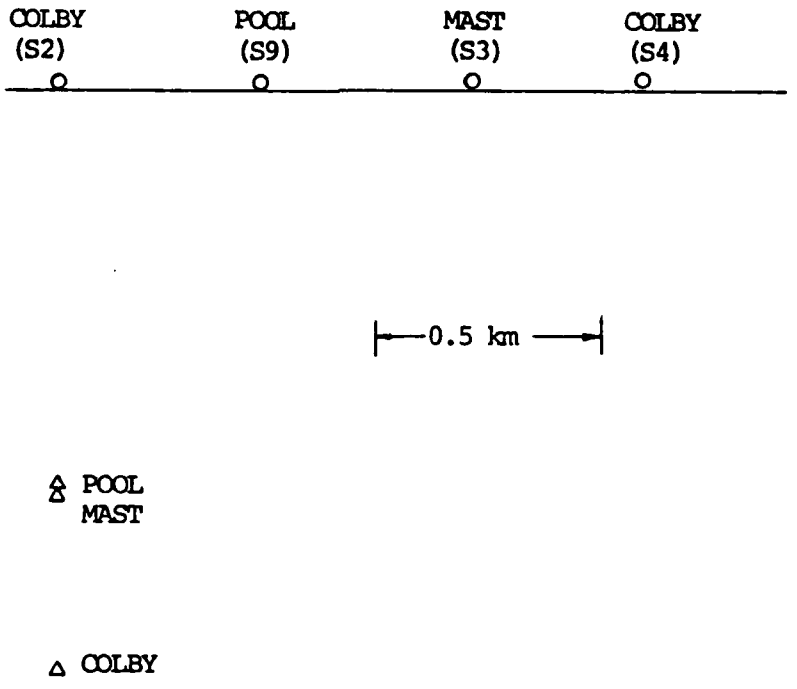

Figure 3.7. Vertical section of geometry for Case II.

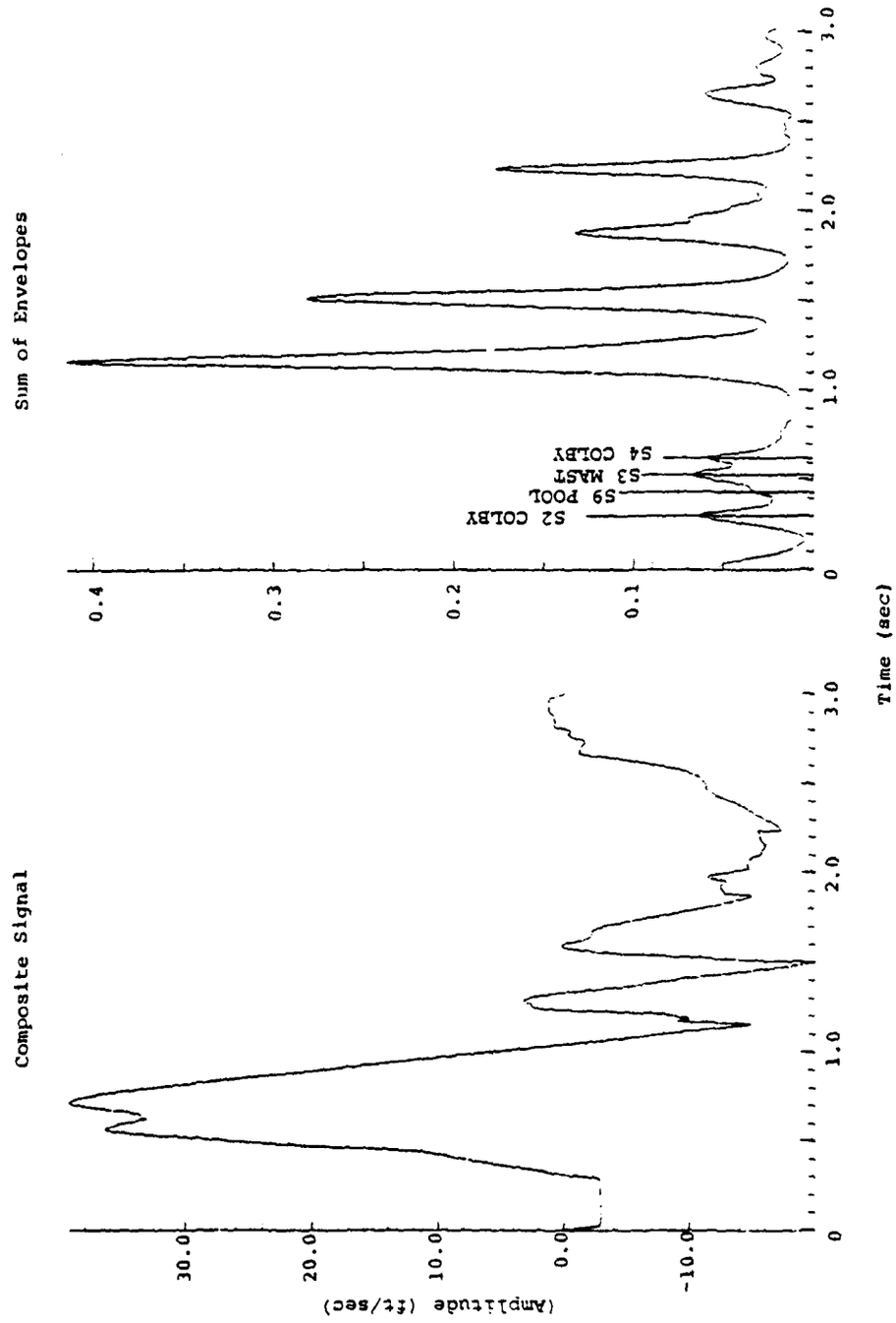

Figure 3.8. Composite signal and Hilbert transform sum for Case II.

peaks (not evident on the composite seismograms) on the envelope sum plot for COLBY S2 and S4 and MAST S3, with a much less distinctive bump for POOL S9. Thus, for the second case, the technique proved successful in separating the arrivals.

These examples and several others are described in our forthcoming topical report. We find that the narrow-band filtering technique would be of great value for identifying and scaling the individual events in a salvo of explosions.

3.3 A LABORATORY SIMULATION OF CRATERING EXPLOSIONS

In our previous quarterly technical report [Bache, et al., 1977], we described some small-scale modeling experiments designed to provide benchmark data for computer simulations of underground explosions. In those experiments, we obtained displacement-time histories on a free surface due to a small spherical charge detonated within a uniform medium of known properties. Our first results were for fully-contained explosions. In our most recent tests, the charge's depth of burial was reduced and cratering occurred.

Figure 3.9 shows the test geometry. The medium, a high-strength concrete, is poured in the form of a right circular cylinder of diameter 122 cm. Over one end of the cylinder, the motion transducers were arrayed at the vertices of a 30 cm equilateral triangle. About 31 cm below each vertex of the triangle, a spherical charge (1/4 gram of PETN) was buried. The charges were fired one at a time, thus each concrete cylinder-transducer setup yielded three complementary sets of data.

Table 3.1 summarizes the experiment matrix, Figures 3.5.1 and 3.5.2 of our previous report show typical results

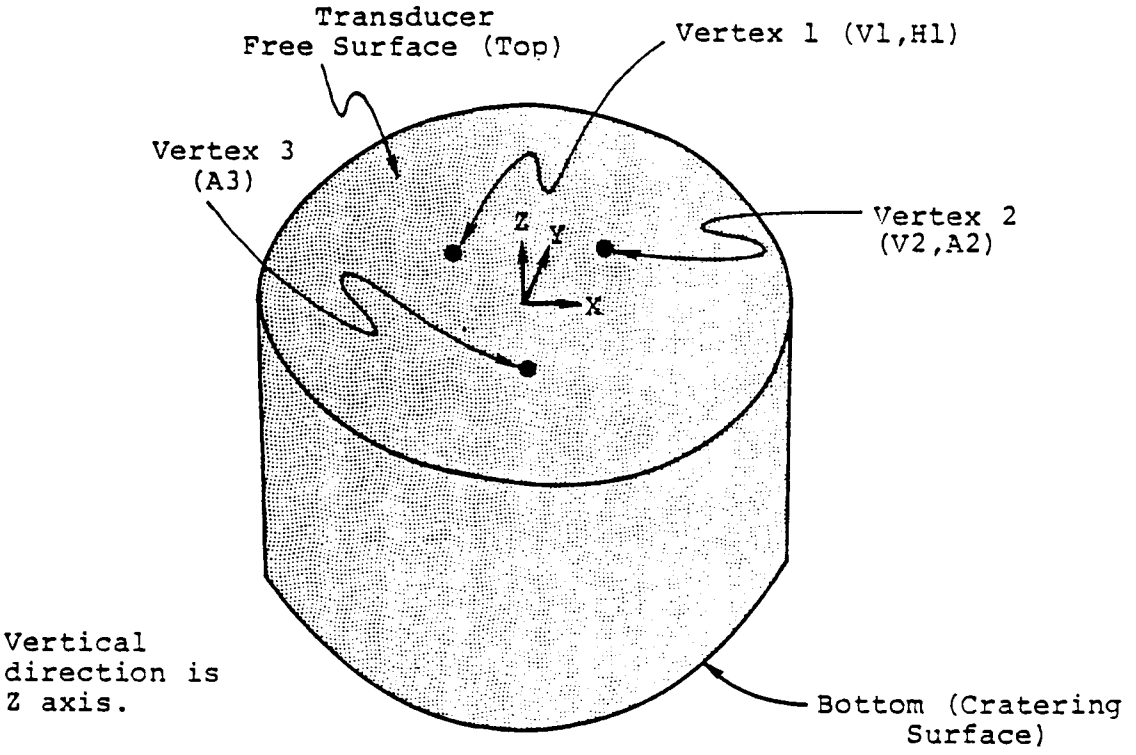

Point	Coordinates (X,Y,Z) cm
Vertex 1	(-15.2, 8.7, 0)
Vertex 2	(15.2, 8.7, 0)
Vertex 3	(0, -17.6, 0)
V1, Vertical Displacement Gauge	(-14.0, 8.7, 0)
H1, Horizontal Displacement Gauge	(-16.5, 8.7, -0.5) Sensitive axis ∥x
V2, Vertical Displacement Gauge	(14.0, 8.7, 0)
A2, Vertical Accelerometer	(16.5, 8.7, 0)
A3, Vertical Accelerometer	(0, -17.6, 0)
Charge 1	(-15.2, 8.7, -31)
Charge 2	(15.2, 8.7, -31)
Charge 3	(0, -17.6, -31)
Cylinder Bottom	(-, -, -33 or -37 or -60 [Table 3.1])

Figure 3.9. Concrete test bed.

TABLE 3.1 SUMMARY OF DETAILS FOR SEISMIC MODELING EXPERIMENTS

Test No.	Cylinder Thickness (cm)	Depth of Charge Burial (cm)	Charge Location (cm)	Crater Surface Dimensions (cm x cm)	Peak Displacement μm (Gauge ID)
1	37	Confined	30.5 cm below Vertex 1	---	5.3 (V1)
2	37	Confined	30.5 cm below Vertex 2	---	3.5 (V2)
3	37	Confined	30.5 cm below Vertex 3	---	5.5 [$\int\int$(A3)dt]
4	60	Confined	30.5 cm below Vertex 1	---	4.9 (V1) (Fig. 3.5.1 of R3108)
5	60	Confined	30.5 cm below Vertex 2	---	3.3 (V2) (Fig. 3.5.2 of R3108)
6	60	Confined	30.5 cm below Vertex 3	---	3.1 [$\int\int$(A3)dt)
7	33	1.75 ±0.08	31.3 cm below Vertex 1	7 x 10	7.0 (V1) (Fig. 14)
8	33	1.43	31.6 cm below Vertex 2	6 x 7	4.9 (V2) (Fig. 15)
9	33	1.91	31.1 cm below Vertex 3	9 x 11	8.5 [$\int\int$(A3)dt) (Fig. 16)

for the contained shots and Figures 3.10-3.12* of the present report give the results for the cratering events. In general, there is good agreement in the wave shapes between the three shots in each configuration, confined or cratering. However, there are differences in absolute amplitudes which are larger than our estimated errors of ±0.3 μm. For the confined shots, we believe these differences are due to slight variations in the coupling between the concrete and the charge surface. For the subsequent cratering tests, our emplacement technique for the charges was improved, and it does appear that the peak displacements are correlated with the crater size and depth of burial. Figure 3.14 shows the measured displacement time history from a contained shot. This displacement gauge was located 30.5 cm from the explosive source. The gauges labeled V1 (Figure 3.10) and V2 (Figure 3.11) measured free field displacement ground motion from an explosive source which produced a crater. The gauges were located 31.3 cm and 31.6 cm from the explosive.

The major difference in the radiated ground motion between the contained and cratering modes (Figures 3.10, 3.11 and 3.14) is the large rebound produced by the cratering shots. This is probably caused by the release of the highly stressed region around the cavity by the free surface reflection. It is very important that this release mechanism be understood in terms of its effect on m_b and M_s.

3.4 NUMERICAL SIMULATION OF MODEL EXPERIMENTS

In our preceding quarterly report [Bache, et al., 1977], we described small-scale experiments which modeled underground

*The error bars shown include the estimated uncertainties due to gauge and recorder calibrations and electrical noise. The figures also quote the times of first arrival and zero crossing and first peaks in the accelerometer records. Integrations of A2's data are not available because of limitations in our recording apparatus.

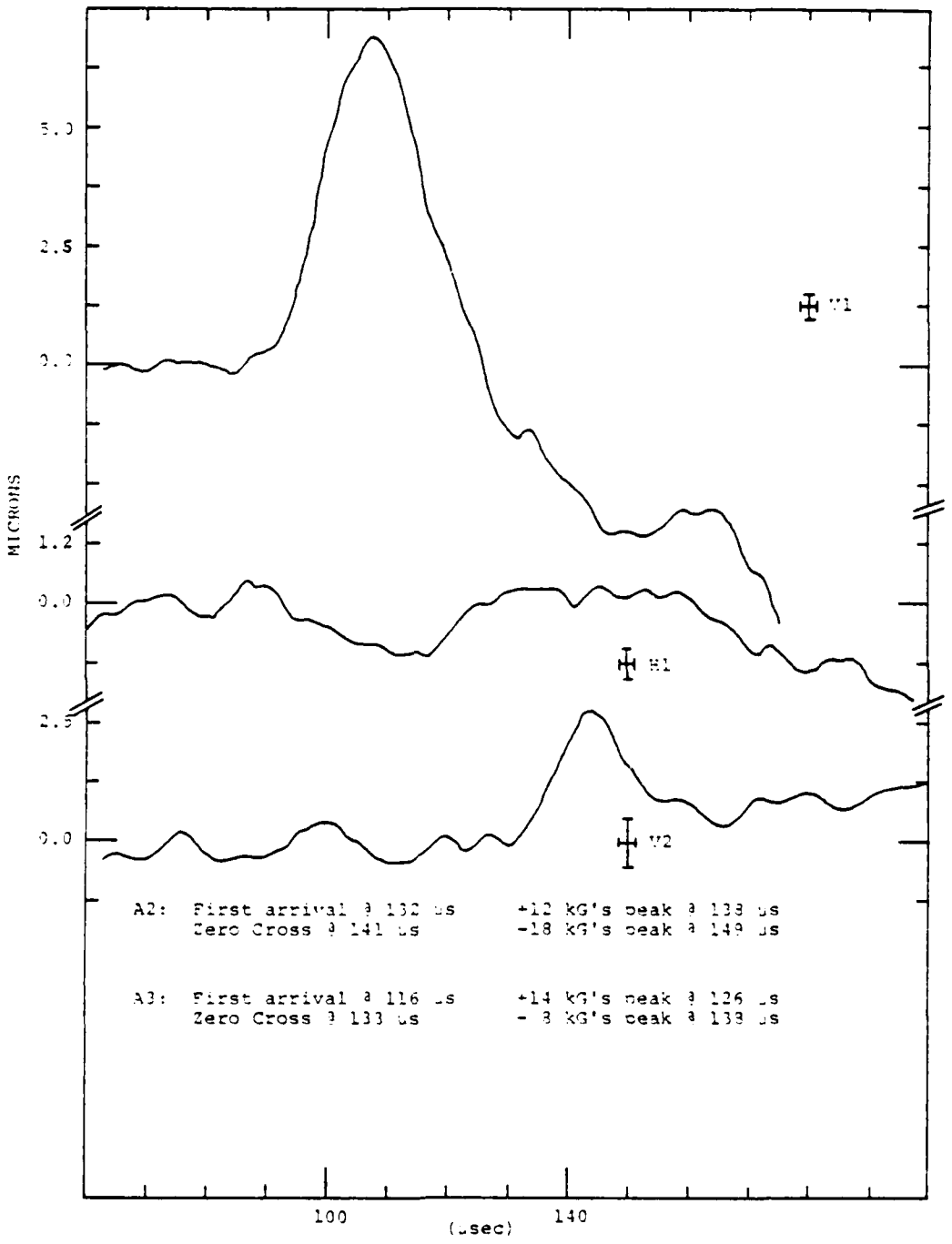

Figure 3.10. Displacement data for charge under Vortex 1 cratering shot (#7).

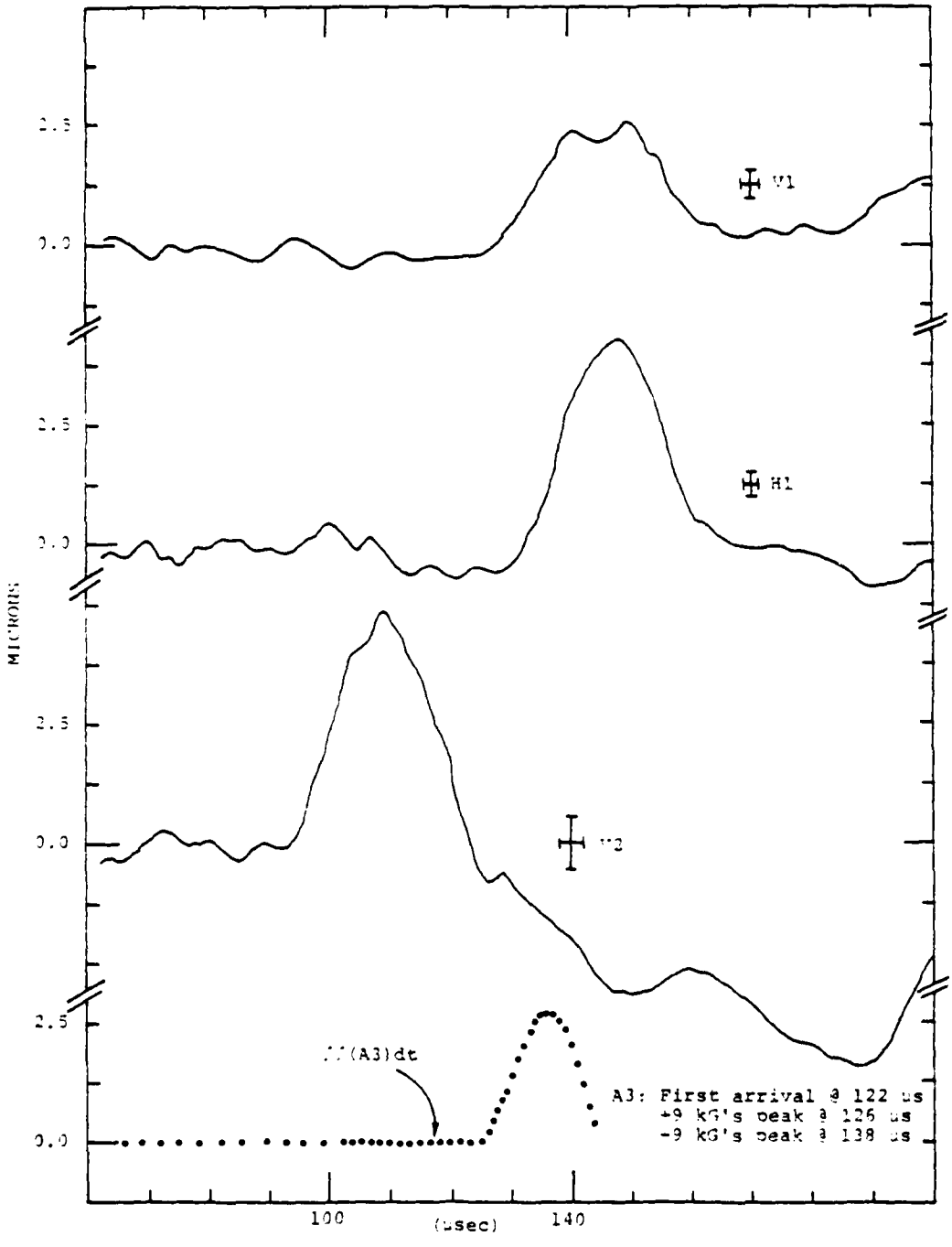

Figure 3.11. Displacement data for charge under Vertex #2 cratering shot (#8).

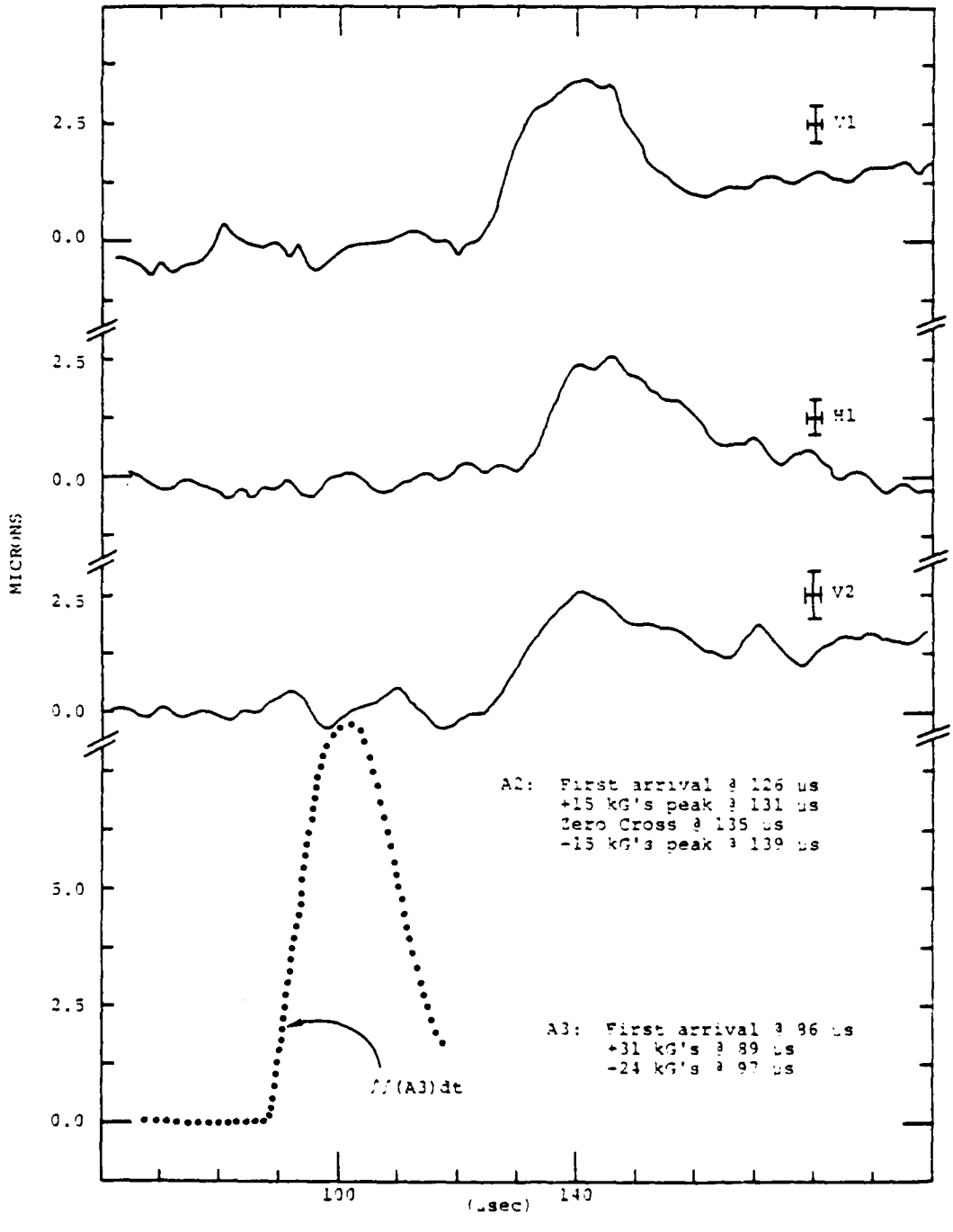

Figure 3.12. Displacement data for charge under Vertex 3 cratering shot (#9).

contained explosions and included measurements of displacement-time histories at the free surface. These experiments have now been numerically simulated using material properties from laboratory measurements and material models most of which were described in an earlier report [Bache, et al., 1975]. One change in the source calculation method was a new effective stress model which does not depend on a relaxation time. The elimination of this time parameter is important for the scaling of source calculations.

The free surface ground motion predicted by the numerical simulation of the model experiments (shown in Figure 3.13) gives excellent agreement with the measured displacement-time histories (Figure 3.14). Only one calculation was done so this agreement was not achieved by a posteriori adjustment of material models or material properties. It therefore provides important confirmation of our source calculation methods. A more complete description of this numerical simulation is given in the following paragraphs.

CONFIGURATION

The model experiments consisted of a spherical 1/4-gram charge of powdered PETN loosely-packed to a density of 1 gm/cm^3. The containing material was "high early" grout formed into a right circular cylinder with a diameter of 120 cm and thickness of 60 cm. The motion was measured at one end of the cylinder and the charges were located 30.5 cm below the surface. Numerically this configuration was modeled as shown in Figure 3.15 with a spherical charge in a sphere of concrete.

GROUT MODELING

The major types of material behavior which we have included in modeling the grout are those attributable to water content, air-filled porosity, brittle failure and plastic

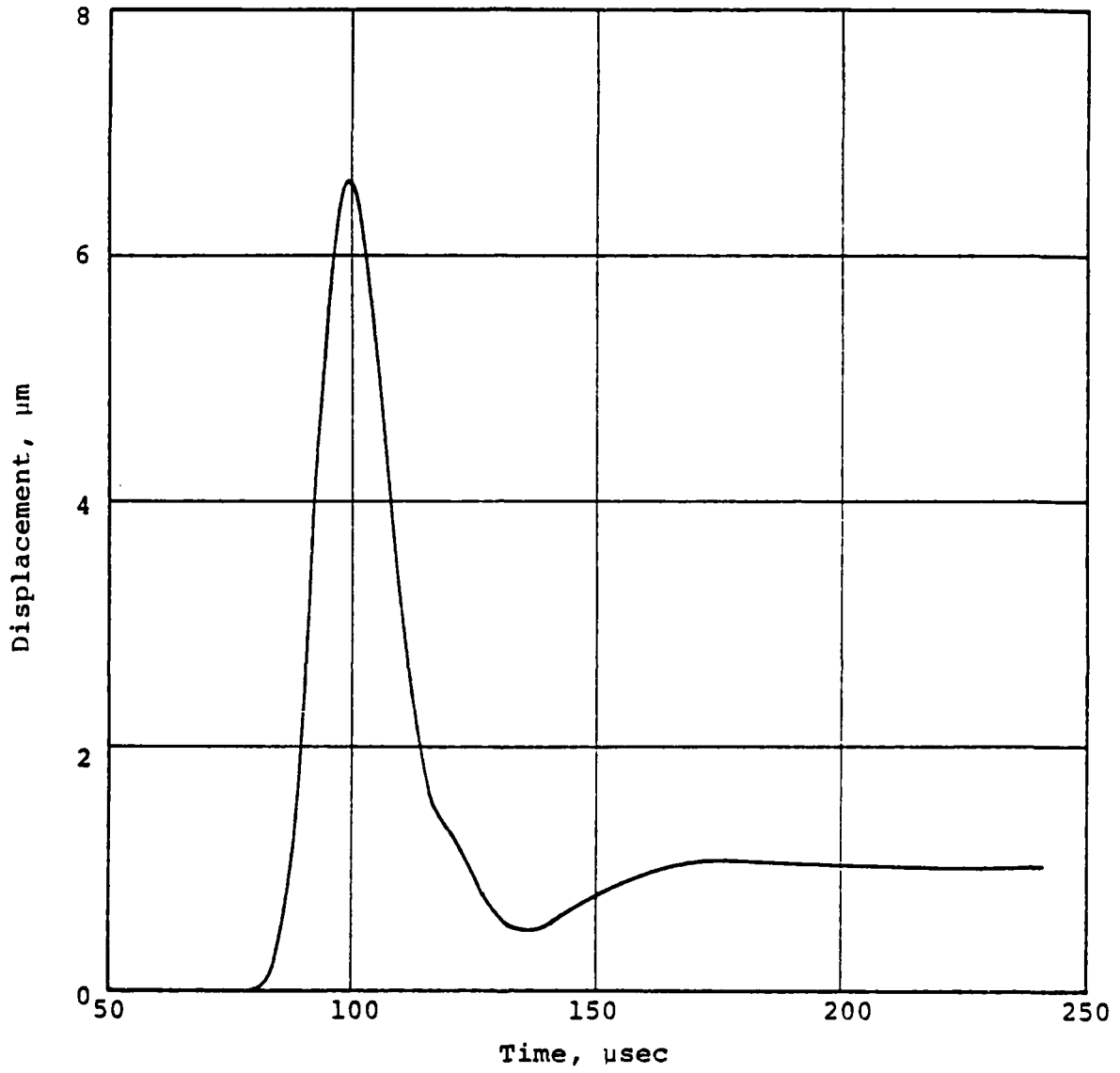

Figure 3.13. Free surface vertical displacement from numerical simulation.

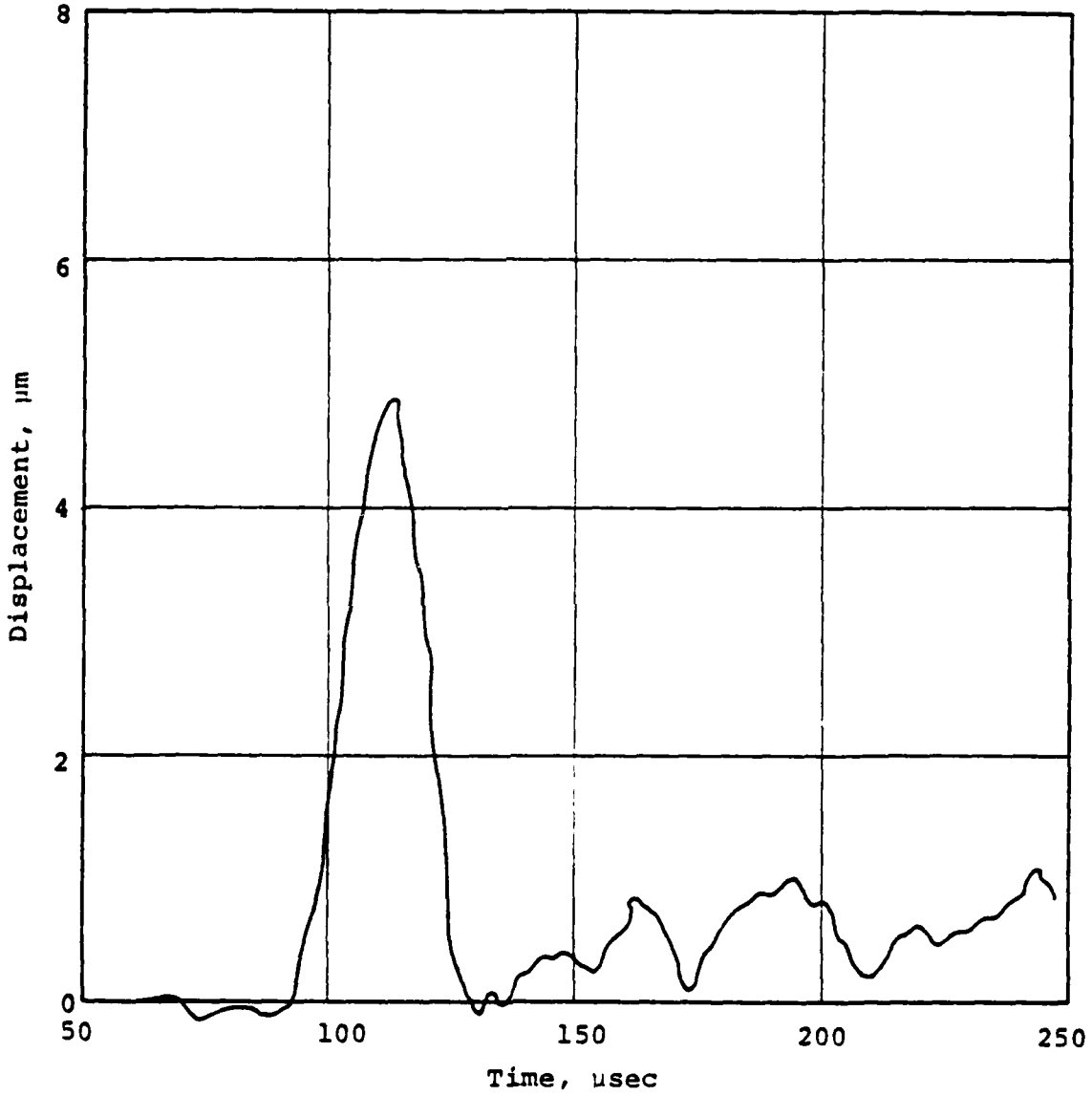

Figure 3.14. Measured vertical free surface displacement.

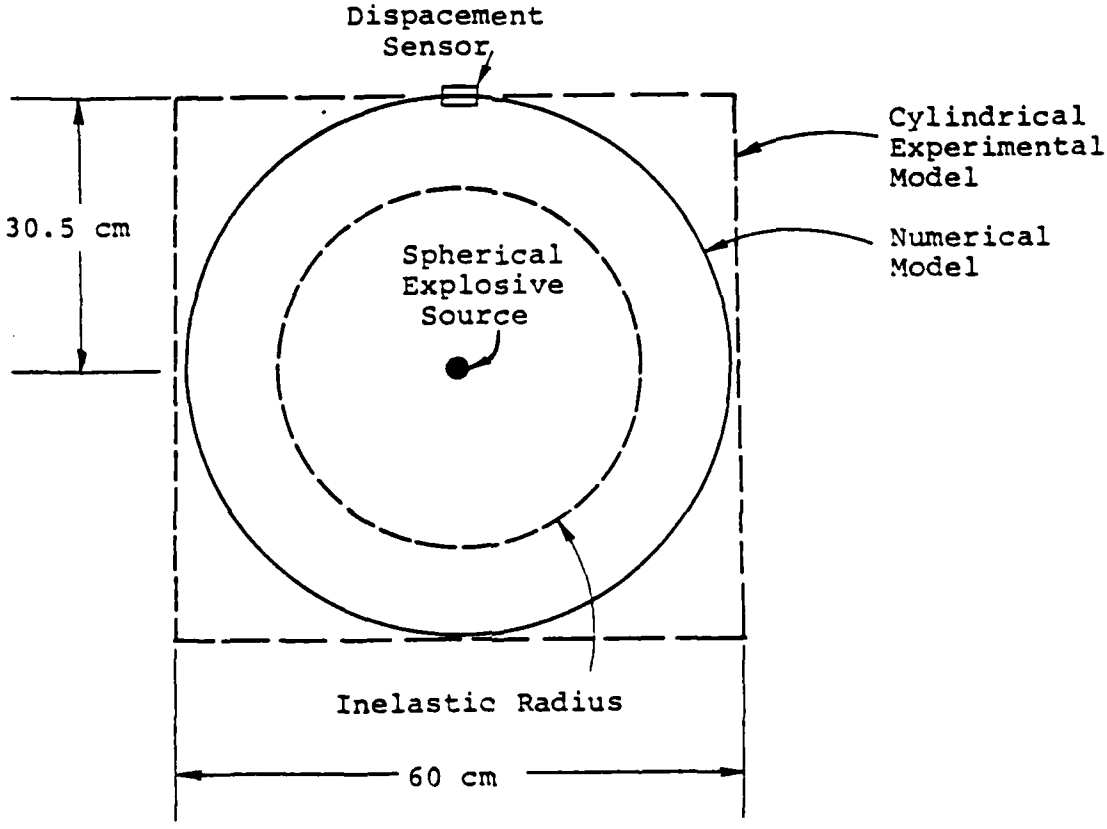

Figure 3.15. Configuration for numerical simulation.

flow. The methods for simulating these phenomena are the same as those described previously [Bache, et al., 1975] except for the treatment of effective stress described below.

The basis of an effective stress law is the assumption that the fluid pressure in fluid saturated rocks should be included in the calculation of the stress state which determines material strength. The definition of stress state, $\bar{P}$, which we have adopted is

$$\bar{P} = P - \frac{1}{2}\left(\frac{J_3'}{2}\right)^{1/3} \tag{3.1}$$

where P is the pressure component of the stress tensor and J_3' is the third deviatoric stress invariant

$$J_3' = (\sigma_{11} + P)\ (\sigma_{22} + P)\ (\sigma_{33} + P) \quad . \tag{3.2}$$

Here, σ_{11}, σ_{22}, σ_{33} are the principal stresses. For our new effective stress method the stress state $\bar{P}$ is adjusted by subtracting the pore fluid pressure, P_f, before the yield function is evaluated. The material strength is determined by the following yield function:

$$Y = Y_0 + \frac{Y_m}{\bar{P}_m}(\bar{P} - P_f)\left[2 - \frac{\bar{P} - P_f}{\bar{P}_m}\right] \quad , \tag{3.3}$$

where $\bar{P}_m$, Y_m and Y_0 are material constants.

The fluid pressure P_f is evaluated as the following function of the crack strains, E_{11}, E_{22}, E_{33}, and the material distension, α, which is the ratio of volume of the solid material to volume of material, including air-filled voids:

$$\alpha_T = \alpha(1 + E_{11} + E_{22} + E_{33}) \quad ,$$

$$P_f = P \text{ for } \alpha_T = 1 \quad ,$$

$$P_f = P \left(\frac{\alpha_T - \alpha_e}{1 - \alpha_e}\right) \text{ for } 1 < \alpha_T < \alpha_e \quad , \tag{3.4}$$

$$P_f = 0 \text{ for } \alpha_T > \alpha_e \quad .$$

In this function, $P_f = P$ for $\alpha_T = 1$ because the fluid pressure is in equilibrium with the rock constituent when all air-filled porosity is removed from the material. For α_T between 1 and the elastic limit, α_e, some of the air-filled porosity has been irreversibly removed and P_f is taken as a linear function of α_T. For $\alpha_T > \alpha_e$ the fluid pressure is zero because the pores are elastically deformed but not irreversibly crushed.

The parameters defining the material behavior for grout for this simulation are summarized in Table 3.2. These parameters were derived from our measurements of the P-wave velocity V_p, density ρ and the unconfined compressive strength Y_u. Additional characteristics were obtained from the extensive data available on DF-5a grout, [Cherry and Peterson, 1970], which is a similar material. In Table 3.1, the parameters A and B define the equation of state in the form

$$A\mu + B\mu^2 \quad ,$$

where $\mu = \frac{\rho}{\rho_o} - 1$. The values for shear modulus, G, and for bulk modulus, A, were determined from V_p and ρ_o by assuming a Poisson's ratio of 0.1, which is appropriate for this type of material.

EXPLOSIVE SOURCE

The explosive source was PETN powder loosely-packed to a density of 1 gm/cm^3. (Solid PETN has an initial density of

TABLE 3.2 MATERIAL PARAMETERS USED FOR HIGH EARLY GROUT

$\rho = 2.52$ gm/cm^3

$Y_u = 0.345$ kbar

$V_p = 3.38 \times 10^5$ cm/sec

$A = 106.5$ kbar

$B = 67.3$ kbar

$Y_o = 0.1725$ kbar

$Y_m = 3$ kbar

$\bar{P}_m = 5$ kbar

$G = 137$ kbar

$P_c = 10$ kbar

$P_e = 0.04$ kbar

1.77 gm/cm^3 and a Chapman-Jouguet density of 2.40 gm/cm^3.) The results of Finger, et al. [1976], provide the values for the constants in the JWL equation of state for the products of detonation of PETN,

$$P = A' \left(1 - \frac{\omega}{R_1 V}\right) e^{-R_1 V} + B' \left(1 - \frac{\omega}{R_2 V}\right) e^{-R_2 V} + \frac{\omega E}{V} , \tag{3.5}$$

and for their isentropic expansion,

$$P_s = A' e^{-R_1 V} + B' e^{-R_2 V} + \frac{C'}{V^{\omega+1}} . \tag{3.6}$$

In Equations (3.5) and (3.6), V is the specific volume, $1/\rho$, and the constants A', B', C', R_1, R_2, and ω are given in Table 3.3.

For the numerical simulation, the source was modeled by a pressure loading function defined by Equation (3.6) and applied at the cavity boundary. The pressure function was started with the PETN detonation products expanded to the actual volume of the loose-packed PETN which corresponds to an initial radius, R_o, of 0.39 cm. Thus, the initial pressure was 31.2 kbar, which is well below the Chapman-Jouguet pressure of 320 kbars.

COMPARISON OF THE RESULTS

The agreement between the measured and calculational results shown in Figures 3.13 and 3.14 is considered to be very good. No adjustment of models or material properties was necessary. The difference between the calculated displacement and the measured displacement is within the range of accuracy of the measurements. This is demonstrated by the

TABLE 3.3 JWL CONSTANTS FOR PETN

$A' = 7960$ kbar

$B' = 192$ kbar

$C' = 6.65$ kbar

$R_1 = 8.50$ gm/cm^3

$R_2 = 2.12$ gm/cm^3

$\omega = 0.25$

$P_{cj} = 320$ kbar

$\rho_{cj} = 2.40$ gm/cm^3

$\rho_o = 1.77$ gm/cm^3

data from a second experiment plotted in Figure 3.16. The displacement time histories shown are from two displacement gauges and a twice-integrated accelerometer record. The three gauges were in close proximity and should be measuring the same motion. The test configuration for these data was the same as that for the data of Figure 3.14 so, from a theoretical point of view, the displacements in Figures 3.14 and 3.16 should be identical. However, the peak displacements range between 4.5 μm and 6.7 μm while the rise time varies between 14 and 20 μsec. Our calculated displacement-time history shows a peak displacement of 6.6 μm and a rise time of 20 μsec.

3.5 REGIONAL SCALING OF SEISMIC AMPLITUDE VERSUS YIELD

The purpose of this section is to describe some preliminary results for research on scaling of seismic amplitudes with yield for nuclear explosions recorded at regional distances (100 to 1000 km). It has been pointed out by Springer and Hannon [1973], that the slope of log amplitude-log yield plots is not unity for Pahute Mesa explosions recorded at regional ranges. Figure 3.17 shows a plot of "b" amplitude versus yield for Pahute Mesa explosions recorded at MINA, Nevada. The b amplitude is measured from the first cycle on the record as shown.

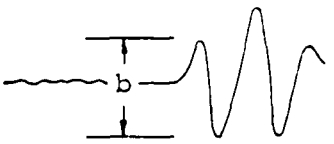

The values on the plot (provided by Lawrence Livermore Laboratory) are amplitudes corrected by the gain of the instrument at 1 Hz, and have not been corrected for the response of the instrument as a function of frequency. A straight line indicating the trend shows that the slopes on the log-log plots are indeed less than one ($\sim$ 0.7).

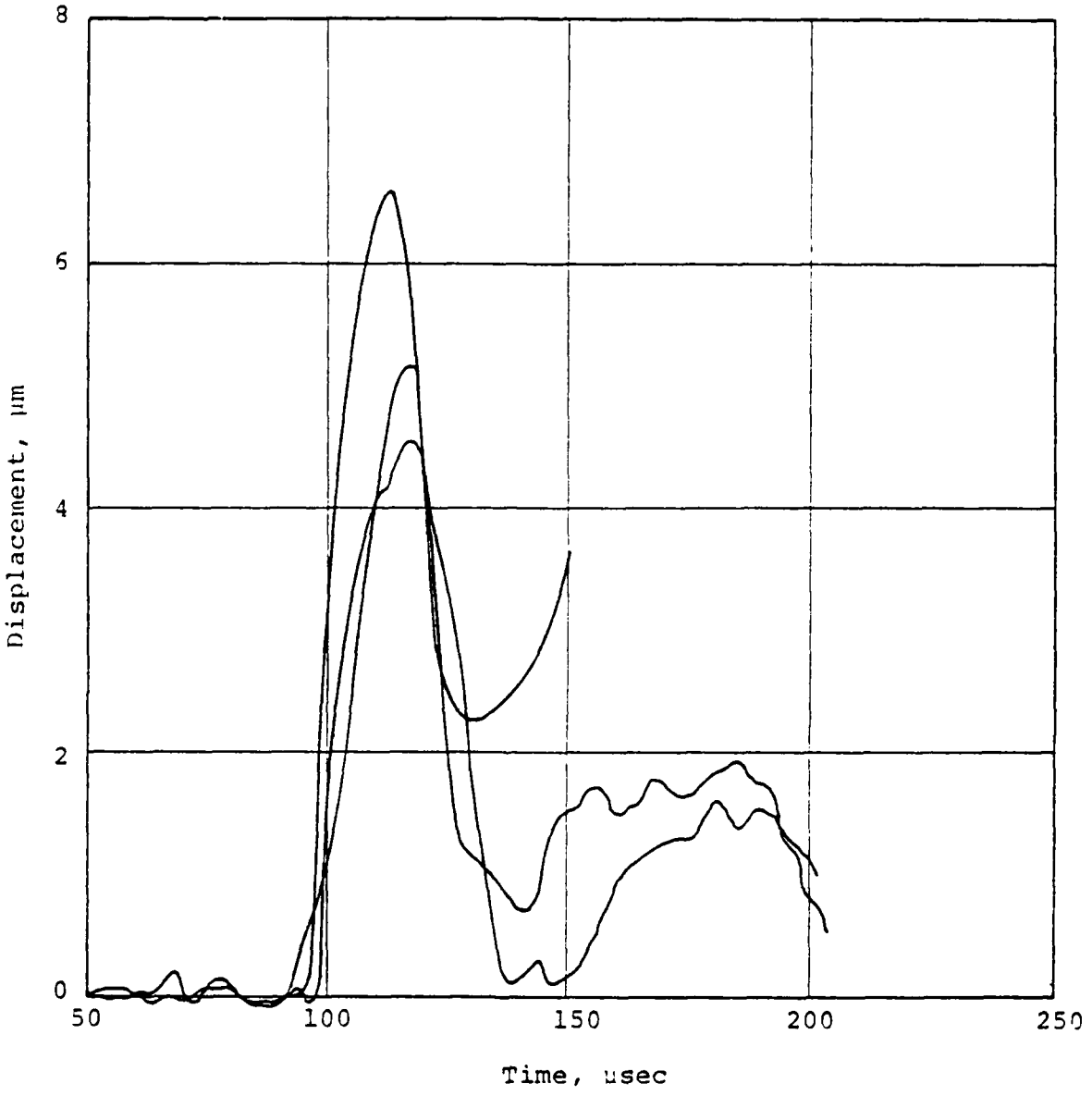

Figure 3.16. Free surface vertical displacement measured in three different ways. The largest peak is from a twice-integrated accelerogram, while the other two displacements are from displacement gauges.

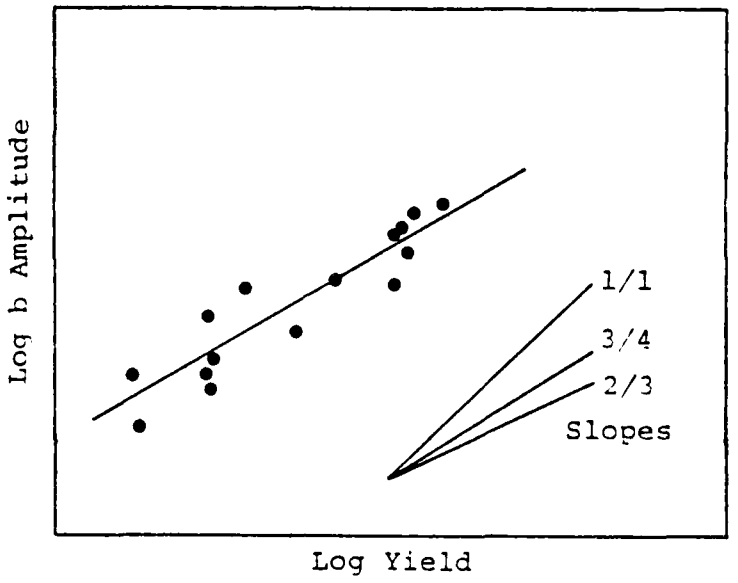

Figure 3.17. Log b versus log yield for Pahute Mesa shots.

Towards understanding this data, the following calculations were done. First, the sources for Pahute Mesa were represented by reduced displacement potentials (RDP) found numerically and used in previous teleseismic amplitude studies [see, e.g., Bache, et al., 1976]. The RDP's at different yields were found by cube root scaling. The RDP's (shown in Figure 3.18) were propagated through a simple earth structure (Figure 3.19) to a range of 200 km using a generalized ray program. The results are then convolved with an LRSM-SP instrument response. Figure 3.20 shows the comparisons of the theoretical results (using source 204) with observations. The slopes are seen to be in good agreement. We shall discuss these comparisons further, but shall first discuss the factors controlling the slope of the log b-log Y curves (hereinafter referred to as versus Y curves).

Several effects contribute to the slopes of the b versus Y curves. The first is the filtering of the signal by the instrument. The short-period instrument behaves as a narrow-band filter centered about 3 Hz. As the yield changes, the instrument samples different parts of the source spectrum. This could be visualized by thinking of the instrument response as fixed, and sliding the source spectrum to the left as yield increases. Thus, the second feature controlling the slope of b versus Y is the shape of the source spectrum. To see this, consider Figure 3.21 in which b versus Y curves are plotted for RDP's of different shape, one being strongly peaked near the corner frequency and one fairly flat. The effects of the crustal structure are not included and the anelastic attenuation factor is $T/Q = 0.1$ for both plots. The curves become parallel at low or high yields but differ markedly for intermediate yields due to the different shape of the source functions near the corner frequency.

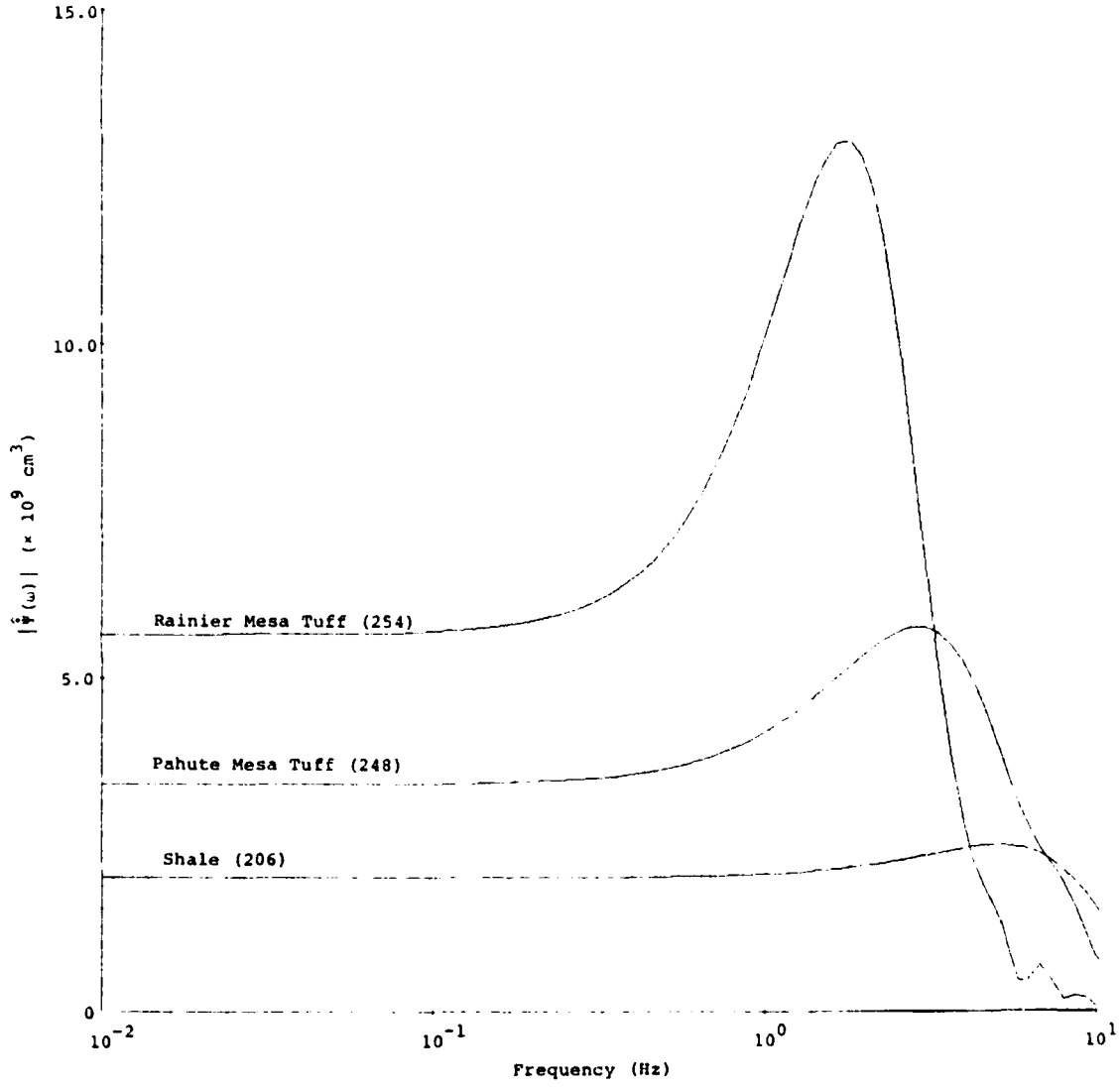

Figure 3.18. Amplitude spectra of reduced displacement potentials for three materials, the amplitude is scaled to 0.02 kt while the frequencies have been scaled to 10 kt.

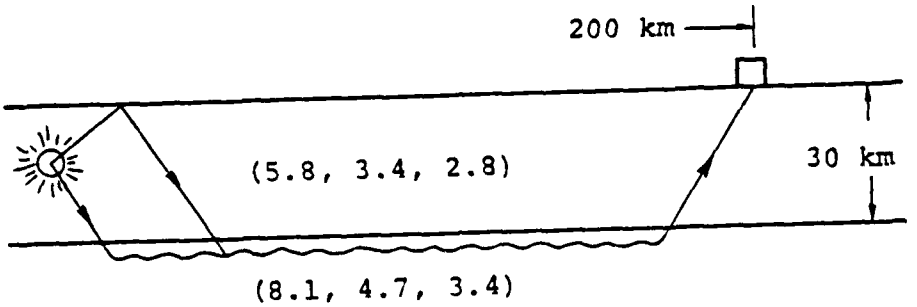

Figure 3.19. Schematic of ray paths and source-receiver geometry. Wavy line indicates a head wave. Vertical traverses are P waves. Values in parentheses are the P and S wave velocity and density.

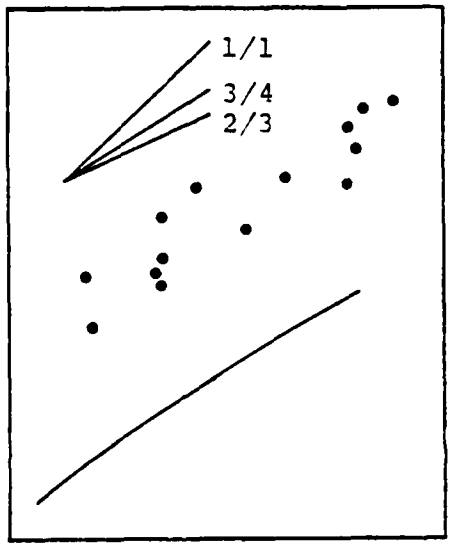

Figure 3.20. Comparison of observed b with calculated b values versus yield.

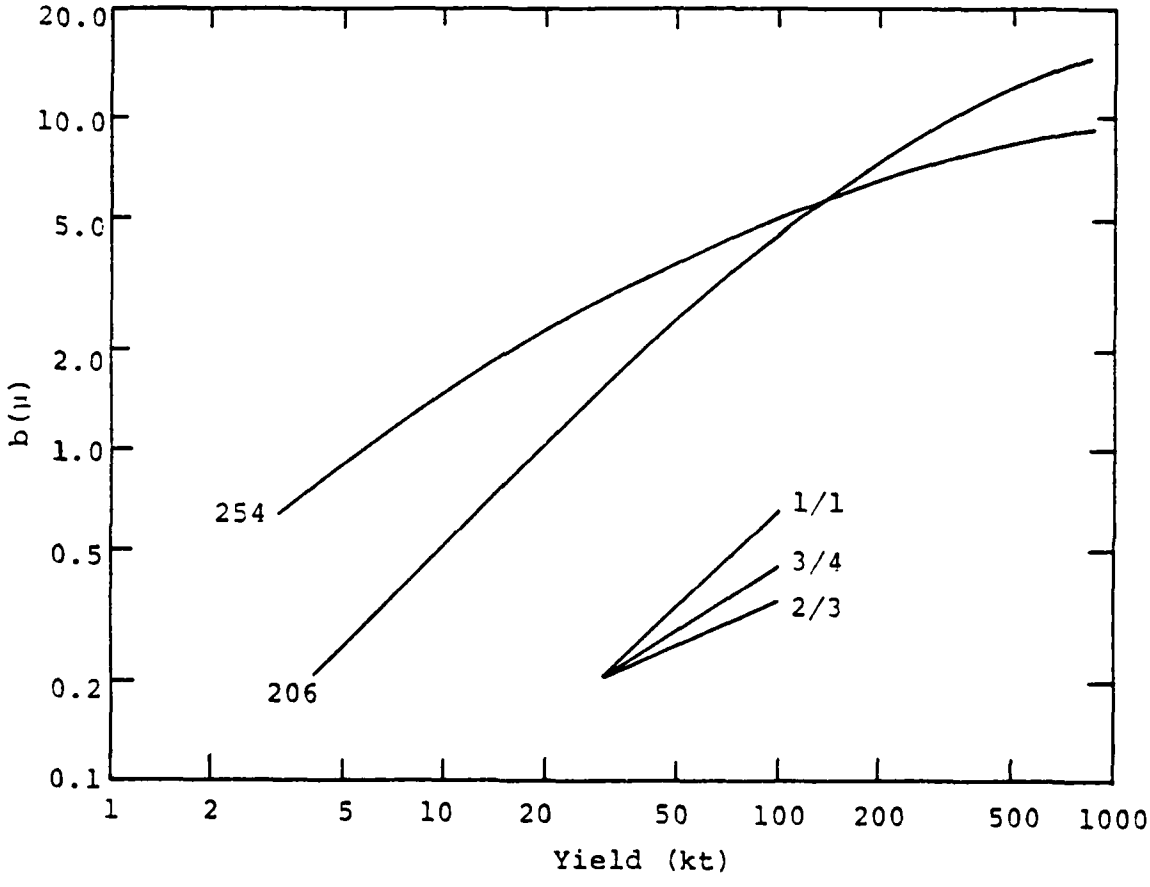

Figure 3.21. Log b versus log yield for sources 206 and 254. The crustal response is not included, and T/Q = 0.1 for both curves.

Another factor controlling the slope of b versys Y curves is the anelastic attenuation. Larger values of T/Q result in greater attenuation of high frequencies relative to low frequencies. Thus, as T/Q increases, amplitudes from lower yield events are attenuated relative to higher yield events, which results in steeper b versus Y curves. Figure 3.22 illustrates the effect of changing T/Q from 0.5 to 0.1 for source 254 with the crustal response removed.

The final feature we shall discuss is the effect of the crustal response. For our simple model at the range 200 km, the response is composed of the head wave from the direct P from the source and the head wave from the free surface reflected (pP) phase (see Figure 3.19). The signal radiated from a head wave at an interface has a time history which is essentially the integral of the incident wave. This is shown in Figure 3.23, where b versus Y curves are plotted, for source 254, with T/Q = 0.1, with and without the crustal response. It can be seen that the slopes are reduced by the crustal response.

We now return to our comparison of the theoretical and observed curves in Figure 3.20. As described above, our theoretical amplitude-yield slope is in close agreement with that of the observations, indicating that the main features controlling the slope have been included in the theoretical model. The theoretical amplitudes are, however, low by a factor of 2 or 3. Considering that no attempt was made to refine crustal models and values of T/Q beyond the first-cut models discussed here, nor to determine the station characteristics of MINA, nor to include effects of depth of burial on source material properties (only cube root scaling was used), this is a reasonable discrepancy. We point out that a number of factors that influence the amplitudes have not been included as yet. The crustal model is extremely simple and only a "first-cut" estimate of Q was used. We will do some

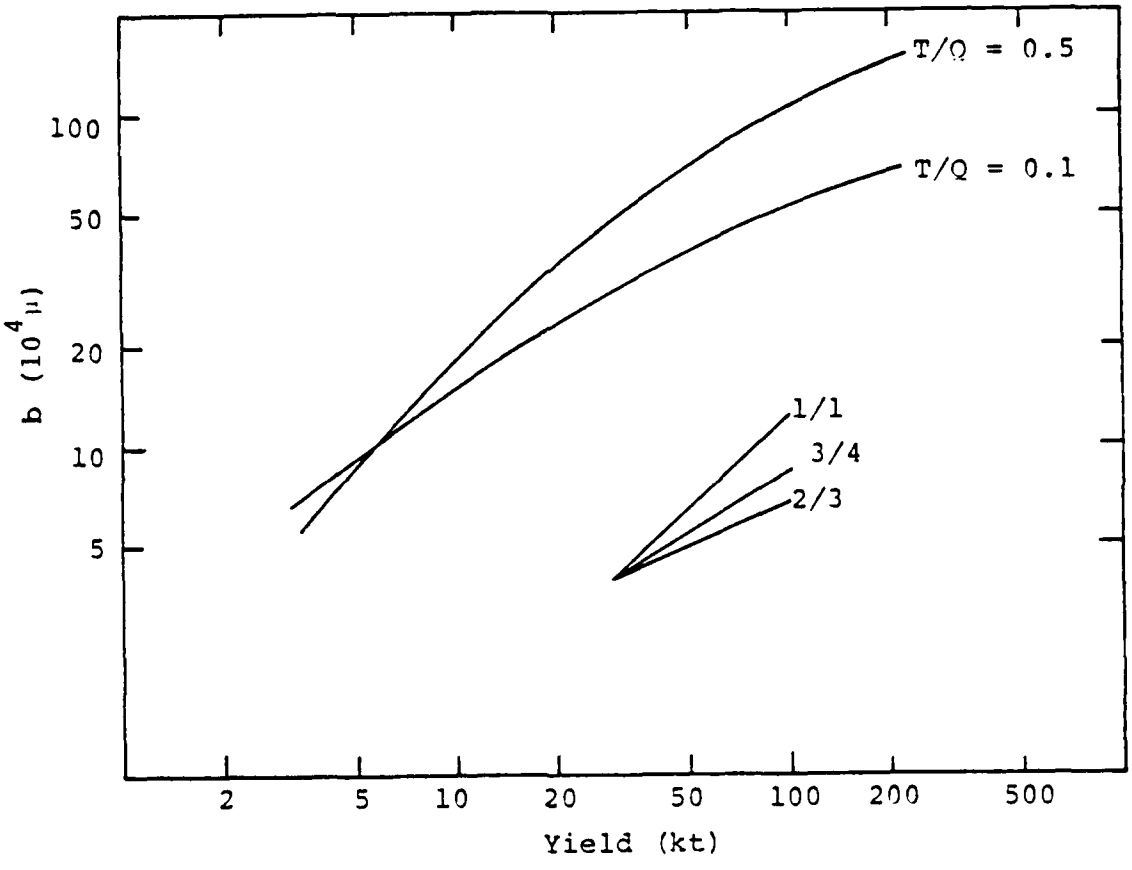

Figure 3.22. Log b versus log yield for source 254 at two different values of T/Q (the curve at T/Q = 0.5 has been multiplied by 10 to facilitate comparison). No crustal response is included.

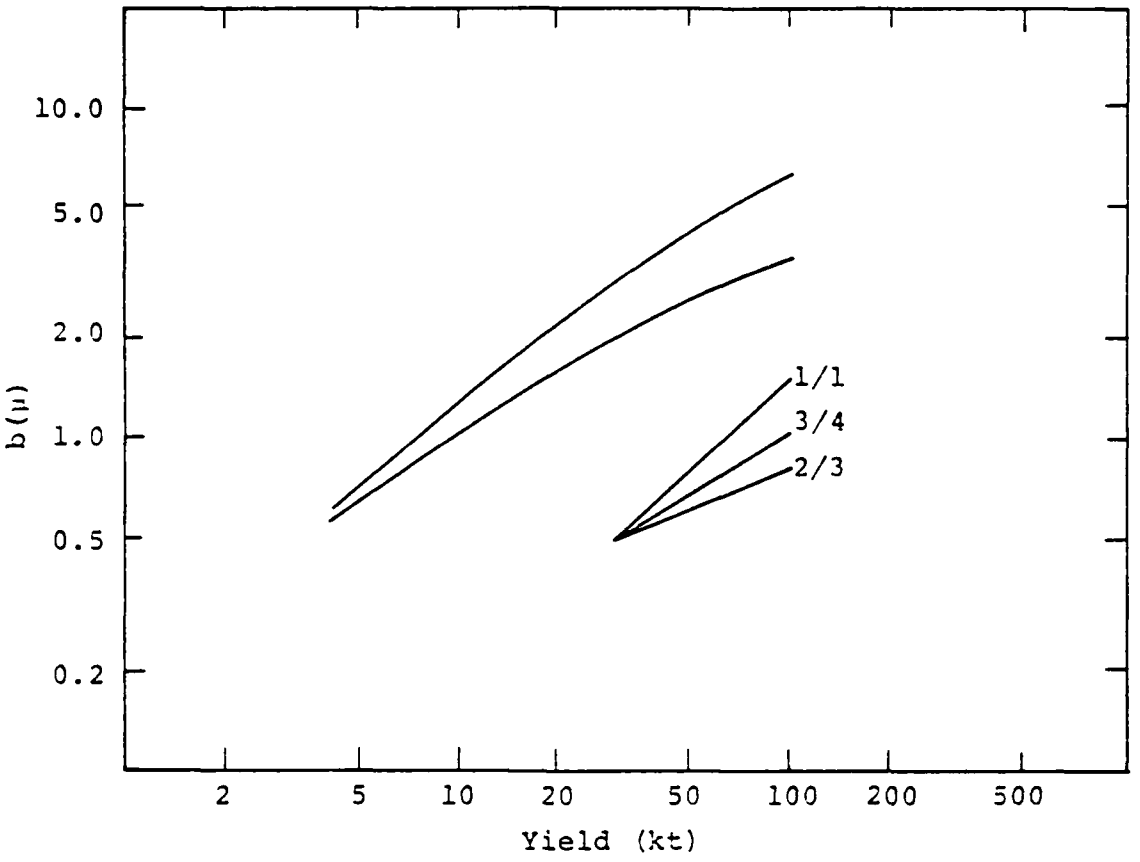

Figure 3.23. Log b versus log yield for source 254, T/Q = 0.1, with (top) and without (bottom) the head wave crustal response. The curves have been shifted vertically for ease of comparison.

calculations in more realistic earth models and also look at data from some of the other regional stations before drawing any conclusions about the agreement of theoretical and observed amplitudes.

REFERENCES

Archambeau, C. B., E. A. Flinn and D. G. Lambert [1969], "Fine Structure of the Upper Mantle," J. Geophys. Res., 74, pp. 5825-5865.

Bache, T. C., J. T. Cherry, N. Rimer, J. M. Savino, T. R. Blake, T. G. Barker and D. G. Lambert [1975], "An Explanation of the Relative Amplitudes Generated by Explosions in Different Test Areas at NTS," Final Contract Report, DNA 3958F, Systems, Science and Software, SSS-R-76-2746.

Bache, T. C., T. G. Barker, J. T. Cherry and J. M. Savino [1976], "Teleseismic Verification of Data Exchange Yields," Systems, Science and Software Topical Report SSS-R-76-2941.

Bache, T. C., J. M. Savino, M. Baker and P. L. Coleman [1977], "Seismic Studies for Improved Yield Determination," Systems, Science and Software Quarterly Report (Draft), SSS-R-77-3108.

Cherry, J. T. and F. L. Peterson [1970], "Numerical Simulation of Stress Wave Propagation from Underground Nuclear Explosions," Engineering with Nuclear Explosions, ANS Topical Meeting, Vol. I.

Finger, M., F. Helm, E. Lee, R. Boat, H. Cheung, J. Walton, B. Hayes and L. Penn [1976], "Characterization of Commercial, Composite Explosives," preprint from The Sixth Symposium on Detonation.

Helmberger, D. V. [1973], "On the Structure of the Low Velocity Zone," Geophys. J. Roy. astr. Soc., 34, pp. 251-263.

Lambert, D. G., C. F. Petersen and J. M. Savino [1976], "Explosion Yield Verification, Multiple Explosion Scenarios and Three-Dimensional Seismic Modeling Research," Systems, Science and Software Quarterly Report (Draft), SSS-R-76-2993.

Lambert, D. G. [1977], Systems, Science and Software Topical Report, in preparation.

Lee, W. B. and S. C. Solomon [1975], "Inversion Schemes for Surface Wave Attenuation and Q in the Crust and the Mantle," Geophys. J. Roy. astr. Soc., 43, pp. 47-71.

Massé, R. P. [1973], "Compressional Velocity Distribution Beneath Central and Eastern North America," Bull. Seism. Soc. Am., 63, pp. 911-935.

Massé, R. P., M. Landisman and J. B. Jenkins [1972], "An Investigation of the Upper Mantle Compressional Velocity Distribution Beneath the Basin and Range Province," Geophys. J. Roy. astr. Soc., 30, pp. 19-36.

Mitchell, J. M. and T. C. Bache [1977], "A Review of the Nature and Variability of the Anelastic Properties of the Upper Mantle Beneath North America and Eurasia," Systems, Science and Software Topical Report (Draft), SSS-R-77-3164.

Savino, J. M., T. C. Bache, T. G. Barker, J. T. Cherry, D. G. Lambert, J. F. Masso, N. Rimer and W. O. Wray [1976], "Improved Yield Determination and Event Identification Research," Systems, Science and Software Final Report (Draft), SSS-R-77-3038.

Springer, D. L. and W. J. Hannon [1973], "Amplitude-Yield Scaling for Underground Nuclear Explosions," Bull. Seism. Soc. Am., 63(2), pp. 477-500.